Generation of tunable and broadband far-infrared laser pulses during two-color filamentation

Francis Théberge,* Marc Châteauneuf, Gilles Roy, Pierre Mathieu, and Jacques Dubois
Defence Research and Development Canada (DRDC) Valcartier, 2459 Pie-XI Boulevard North, Québec G3J 1X5, Canada
(Received 16 November 2009; published 11 March 2010)

Tunable far-infrared laser pulses were generated efficiently during two-color filamentation in air. Understanding the creation of few-cycle far-infrared laser pulses is important since it is at the frontier between two possible generation mechanisms. The first one is the four-wave mixing generation, associated to the generation of wavelengths from ultraviolet up to mid-infrared laser pulses. The second process is the formation of transient photocurrent, which was recently used to describe the generation of submillimetric (terahertz) waves. Comparison between experiments and simulations revealed that the four-wave mixing mechanism is dominant for the far-infrared generation during two-color filamentation.

DOI: 10.1103/PhysRevA.81.033821 PACS number(s): 42.65.Jx, 32.80.Fb, 52.38.Kd

Filamentation of ultrashort laser pulses demonstrated numerous potential applications such as guiding electric discharges [1] and microwaves [2], the compression of few-cycle and powerful laser pulses [3], and the generation of ultrabroadband white-light laser [4,5] and its application to the teledetection of atmospheric pollutants [6]. Filamentation of ultrashort laser pulses in optical media is governed by the dynamic interplay among the optical Kerr effect due to the intensity-dependent refractive index, the intrinsic diffraction of the laser beam, and defocusing from low-density plasma induced by multiphoton/tunnel ionization [7–9]. During nonlinear propagation, the laser self-transforms into a white-light laser pulse and the interaction between the spectral components of this filamenting pulse can also contribute to its spectral broadening [5] up to the generation of a submillimetric (terahertz) pulse [10]. However, the copropagation of two pump pulses of different wavelengths in the filament zone was shown to be a simple and more efficient method of generating new broadband pulses through third-order nonlinear processes. These nonlinear interactions occurring in the core of filament produced new laser pulses having peak wavelength from the ultraviolet (UV) [11] up to the mid-infrared (MIR) [12,13]. Recently, broadband terahertz pulse generation has also been reported by using two-color pump pulses [14–16]. While the gap of the far-infrared (FIR) wavelength was not studied through two-color filamentation, the reported mechanisms describing the generation of laser pulses from UV to MIR and in the terahertz band are different. The generation of UV up to MIR laser pulses during two-color filamentation has been described through the four-wave mixing (4WM) parametric generation [11–13]. Such a process was attributed to the nonlinear response of neutral atoms and molecules in the high-intensity zone of the filament. On the other hand, the generation of broadband terahertz (THz) pulses spanning down to the FIR was attributed to a transient photocurrent induced by the free electrons driven by the asymmetric field of the pump pulses [15]. Since the generation of FIR pulses during two-color filamentation is bridging the gap separating the two generation mechanisms, it becomes important to clarify the physical process involved.

The experiment was performed using the Terawatt & Terahertz portable laser facility producing laser pulses of 5 TW peak power at a repetition rate of 10 Hz. The laser system delivers 225 mJ per pulse with a pulse duration of 38 fs. The central wavelength is 805 nm and the spectral bandwidth is 27 nm. The compact Ti:sapphire laser system sits on a $1.25 \times 2.5\text{-m}^2$ optical table which is mounted inside a sea container that can be transported in the field. For the experiments reported here, the diameter of the beam at the output of the optical compressor was 2.5 cm at full width half maximum (FWHM). The key element of the experiment was to split the original beam into two beams having different central wavelengths. The first beam is frequency doubled by a second harmonic crystal and is combined with the second beam in order to create the two-color filamentation. The splitting of the beam was done with a dichroic mirror (DM1) having a smooth cutoff reflectivity at 805 nm. Thus, this mirror reflected the spectral components below 805 nm and transmitted the wavelengths longer than 805 nm. The two resulting beams had equal energy, but different spectral distributions [see Fig. 1(b)]. The laser beam centered at 795 nm was used to generate a filament in air, while the 813-nm beam propagated in an optical delay line and through a 500-μm-thick potassium dihydrogen phosphate (KDP) crystal used as second harmonic (SH) generator. Such a thick KDP crystal had a SH conversion efficiency of 5% for the 813-nm laser beam. The resulting spectral narrowing of the SH pulse due to the thickness of the KDP crystal had negligible impact on this experiment. The SH pulse was superimposed concentrically with the 795-nm laser pulse by a second dichroic mirror (DM2). The DM2 transmitted the SH beam, reflected the 795-nm pulse on its front surface and rejected the residual 813-nm pump beam at its rear surface. The temporal delay between the SH and the 795-nm laser pulses was controlled by the optical delay line. The two beams were focused in ambient air with a silver-coated concave mirror (CM) having a 1.5-m-long focal length. The polarization of the two beams was individually controlled with half-wave ($\lambda/2$) and quarter-wave ($\lambda/4$) plates. Before the filament, the pulse duration of the near-infrared (NIR) (795 nm) pulse was 50 fs at FWHM (transform limited), while the SH pulse was positively chirped to 130 fs (transform-limited pulse duration was 70 fs).

After the two-color filamentation, the spectra of the NIR and SH pulses were both slightly affected by the nonlinear

*Corresponding author: francis.theberge@drdc-rddc.gc.ca

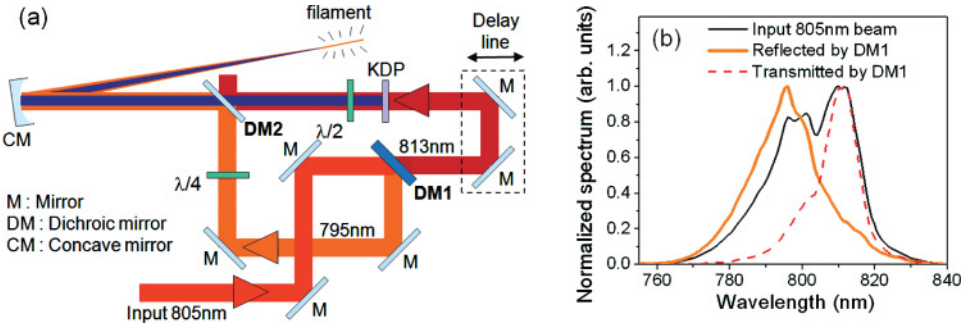

FIG. 1. (Color online) (a) Experimental setup for the generation of a far-infrared pulse during filamentation in air. (b) Spectral distribution of the laser pulses before and after the dichroic mirror DM1.

interaction occurring in the filament. In the case of the SH pulse, we observed a symmetric spectral broadening which was due to the self-phase modulation and the cross-phase modulation with the NIR pulse. For the NIR pump pulse, we observed a predominant blue-shift broadening which was due to the self-steepening [7–9], and the centroid wavelength shifted to 785 nm.

A third pulse in the FIR was also generated during the two-color filamentation. This FIR pulse was isolated with a 5-mm-thick germanium window positioned 50 cm beyond the filament. The germanium window reflected and absorbed the pump pulses and transmitted the IR wavelength from 2 μm up to at least 15 μm. The spectral distribution of the FIR pulse was characterized by a calibrated monochromator using a liquid-nitrogen-cooled mercury-cadmium-telluride detector. Figure 2(a) presents the measured spectral distribution of the generated FIR pulse as a function of the relative delay between the linearly polarized NIR and SH pump pulses. The spectral distribution of the FIR pulse is shown in Figs. 2(b)–2(e) for some specific delays. It is interesting to note that since the SH pulse was chirped, it was thus possible to control the peak wavelength of the generated FIR pulse by varying the delay between the pump pulses. In Fig. 2(c), the peak wavelength of the FIR pulse is 10.5 μm and the spectral width is 2.2 μm at FWHM. Although the initial chirp of the SH pulse is expected to be transferred to the FIR pulse, the spectral width of the latter

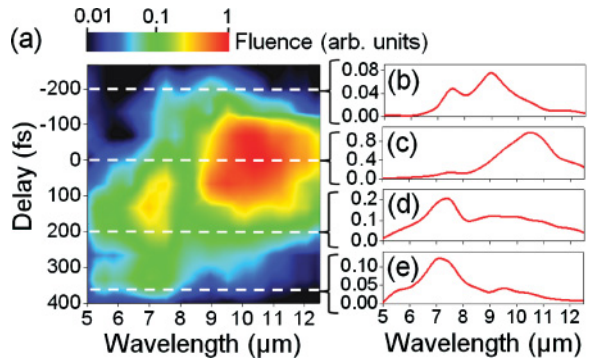

FIG. 2. (Color online) (a) FIR spectrum generated during the cofilamentation in air of a 20-mJ NIR laser pulse and a 1-mJ SH laser pulses. The vertical axis is the relative delay between the pump pulses. A positive delay corresponds to the SH pulse in front of the NIR pulse and vice-versa for the negative delay. The zero delay was arbitrarily set to the optimum FIR energy. The false colors associated with the spectrum are related to the relative spectral fluence. The white dashed lines indicate the delay of the measured spectrum for (b) −200 fs, (c) 0 fs, (d) +200 fs, and (e) +365 fs.

can support a Fourier transform-limited pulse duration of 75 fs (FWHM), which corresponds to a 2.1-cycle laser pulse at 10.5 μm. Similarly in Fig. 2(d), the FIR spectrum is centered at 8.5 μm and its bandwidth increased to 4.1 μm; such a broadband FIR pulse sustains a transform-limited pulse duration of 30 fs, which corresponds to a single-cycle FIR laser pulse.

The generation of such a broadband FIR pulse during the two-color filamentation could either be explained through the 4WM [13] or the photocurrent models [15]. The 4WM model describes the FIR-pulse generation through the $\chi^{(3)}$ nonlinear intensity response where the local nonlinear polarization (P^{NL}) of the three pulses propagating in a centrosymmetric medium is given by

$$
\begin{aligned}
P^{\mathrm{NL}}_{k,\mathrm{FIR}} &= \big[\chi^{(3)}_{kkkk}E^{\mathrm{NIR}}_{k}E^{\mathrm{NIR}}_{k}E^{\mathrm{SH}^*}_{k} + \chi^{(3)}_{kjkj}E^{\mathrm{NIR}}_{j}E^{\mathrm{NIR}}_{k}E^{\mathrm{SH}^*}_{j} \\
&\quad + \chi^{(3)}_{kjjk}E^{\mathrm{NIR}}_{j}E^{\mathrm{NIR}}_{j}E^{\mathrm{SH}^*}_{k} + \chi^{(3)}_{kkjj}E^{\mathrm{NIR}}_{k}E^{\mathrm{NIR}}_{j}E^{\mathrm{SH}^*}_{j}\big] \\
&\quad + \big[\chi^{(3)}_{kkkk}E^{\mathrm{FIR}^*}_{k}E^{\mathrm{FIR}}_{k}E^{\mathrm{FIR}}_{k} + \chi^{(3)}_{kjjk}E^{\mathrm{FIR}^*}_{j}E^{\mathrm{FIR}}_{j}E^{\mathrm{FIR}}_{k}\big] \\
&\quad + 2\big[\chi^{(3)}_{kkkk}E^{\mathrm{SH}^*}_{k}E^{\mathrm{SH}}_{k}E^{\mathrm{FIR}}_{k} + \chi^{(3)}_{kkkk}E^{\mathrm{NIR}^*}_{k}E^{\mathrm{NIR}}_{k}E^{\mathrm{FIR}}_{k} \\
&\quad + \chi^{(3)}_{kjjk}E^{\mathrm{SH}^*}_{j}E^{\mathrm{SH}}_{j}E^{\mathrm{FIR}}_{k} + \chi^{(3)}_{kjjk}E^{\mathrm{NIR}^*}_{j}E^{\mathrm{NIR}}_{j}E^{\mathrm{FIR}}_{k}\big], \\
P^{\mathrm{NL}}_{k,\mathrm{NIR}} &= 2\big[\chi^{(3)}_{kkkk}E^{\mathrm{SH}}_{k}E^{\mathrm{FIR}}_{k}E^{\mathrm{NIR}^*}_{k} + \chi^{(3)}_{kjkj}E^{\mathrm{SH}}_{j}E^{\mathrm{FIR}}_{k}E^{\mathrm{NIR}^*}_{j} \\
&\quad + \chi^{(3)}_{kjjk}E^{\mathrm{SH}}_{j}E^{\mathrm{FIR}}_{j}E^{\mathrm{NIR}^*}_{k} + \chi^{(3)}_{kkjj}E^{\mathrm{SH}}_{k}E^{\mathrm{FIR}}_{j}E^{\mathrm{NIR}^*}_{j}\big] \\
&\quad + \big[\chi^{(3)}_{kkkk}E^{\mathrm{NIR}^*}_{k}E^{\mathrm{NIR}}_{k}E^{\mathrm{NIR}}_{k} + \chi^{(3)}_{kjjk}E^{\mathrm{NIR}^*}_{j}E^{\mathrm{NIR}}_{j}E^{\mathrm{NIR}}_{k}\big] \\
&\quad + 2\big[\chi^{(3)}_{kkkk}E^{\mathrm{SH}^*}_{k}E^{\mathrm{SH}}_{k}E^{\mathrm{NIR}}_{k} + \chi^{(3)}_{kkkk}E^{\mathrm{FIR}^*}_{k}E^{\mathrm{FIR}}_{k}E^{\mathrm{NIR}}_{k} \\
&\quad + \chi^{(3)}_{kjjk}E^{\mathrm{SH}^*}_{j}E^{\mathrm{SH}}_{j}E^{\mathrm{NIR}}_{k} + \chi^{(3)}_{kjjk}E^{\mathrm{FIR}^*}_{j}E^{\mathrm{FIR}}_{j}E^{\mathrm{NIR}}_{k}\big], \\
P^{\mathrm{NL}}_{k,\mathrm{SH}} &= \big[\chi^{(3)}_{kkkk}E^{\mathrm{NIR}}_{k}E^{\mathrm{NIR}}_{k}E^{\mathrm{FIR}^*}_{k} + \chi^{(3)}_{kjkj}E^{\mathrm{NIR}}_{j}E^{\mathrm{NIR}}_{k}E^{\mathrm{FIR}^*}_{j} \\
&\quad + \chi^{(3)}_{kjjk}E^{\mathrm{NIR}}_{j}E^{\mathrm{NIR}}_{j}E^{\mathrm{FIR}^*}_{k} + \chi^{(3)}_{kkjj}E^{\mathrm{NIR}}_{k}E^{\mathrm{NIR}}_{j}E^{\mathrm{FIR}^*}_{j}\big] \\
&\quad + \big[\chi^{(3)}_{kkkk}E^{\mathrm{SH}^*}_{k}E^{\mathrm{SH}}_{k}E^{\mathrm{SH}}_{k} + \chi^{(3)}_{kjjk}E^{\mathrm{SH}^*}_{j}E^{\mathrm{SH}}_{j}E^{\mathrm{SH}}_{k}\big] \\
&\quad + 2\big[\chi^{(3)}_{kkkk}E^{\mathrm{NIR}^*}_{k}E^{\mathrm{NIR}}_{k}E^{\mathrm{SH}}_{k} + \chi^{(3)}_{kkkk}E^{\mathrm{FIR}^*}_{k}E^{\mathrm{FIR}}_{k}E^{\mathrm{SH}}_{k} \\
&\quad + \chi^{(3)}_{kjjk}E^{\mathrm{NIR}^*}_{j}E^{\mathrm{NIR}}_{j}E^{\mathrm{SH}}_{k} + \chi^{(3)}_{kjjk}E^{\mathrm{FIR}^*}_{j}E^{\mathrm{FIR}}_{j}E^{\mathrm{SH}}_{k}\big].
\end{aligned}
\tag{1}
$$

Here the subscripts k and j denote the electric field (E) component along the x and y axes, where $k = x, y$ and $j = y, x$, and the propagation direction is along the z axis. For each expression of the nonlinear polarization in Eq. (1), the first bracket stands for the source term generating the corresponding frequency (ω_{FIR}, ω_{NIR}, or ω_{SH}). The second bracket corresponds to the self-phase modulation and the third bracket is related to the cross-phase modulation induced

by the two other pulses. These nonlinear polarizations were introduced in a set of three coupled equations very similar to the ones given in Ref. [17], which considers the geometrical focusing, diffraction, group-velocity dispersion, and electronic $\chi^{(3)}$ response. Electron generation through multiphoton ionization of N_2 and O_2 is taken into account only for the NIR pulse and the ionization rates are fitted into the form σI^n for the relevant intensity range [18], where σ is the cross section for the multiphoton ionization, n is the multiphoton parameter, $I = c\varepsilon_0[(E_x^{\mathrm{NIR}})^2 + (E_y^{\mathrm{NIR}})^2]$ corresponds to the instantaneous NIR intensity, c is the speed of light, and ε_0 is the vacuum permittivity.

Alternatively, according to the photocurrent model, the FIR pulse originates from a transient current induced by the laser acceleration of free electrons in the core of the filament [15]. During the two-color filamentation, the local photocurrent $[J(t)]$ induced by the electric field of the pump pulses is given by

$$J(t) = \int_{t_0}^{t} e^2\{[E^{\mathrm{SH}}(t)/m_e\omega_{\mathrm{SH}}] + [E^{\mathrm{NIR}}(t)/m_e\omega_{\mathrm{NIR}}]\}N_e(t')dt', \quad (2)$$

where e, m_e, and N_e are the electron charge, mass, and density, respectively. The spectral amplitude of the generated FIR pulse is then related to the time derivative and the Fourier transform of this photocurrent, according to

$$E^{\mathrm{FIR}}(\omega_{\mathrm{FIR}}) = \int_{-\infty}^{+\infty} [dJ/dt]\exp(i\omega_{\mathrm{FIR}}t)dt. \quad (3)$$

It should be noted that in the case of FIR-pulse generation with the photocurrent model, the FIR pulse generated is not due to the production of a net current perpendicular to the propagation axis as for the case of THz generation [15]. In fact, the FIR pulse originates from the beating of this photocurrent induced by the interference of the 785- and 407-nm laser fields (see Fig. 3).

Simulations demonstrated that the FIR-pulse generation efficiencies calculated using these two models are insensitive to a variation of the relative delay of $\lambda_{\mathrm{SH}}/2$ between the SH and the NIR pulses as observed in Ref. [15], but the FIR efficiencies have a distinctive dependency on the polarization state of these pump pulses. Based on this difference, the experimental result of the measured FIR energy as a function of the pump pulse polarization was used to identify the dominant mechanism for the FIR-pulse generation during the two-color filamentation.

In the experimental setup, the focusing condition of the pump and probe beams (f number $= 60$) results in a peak plasma density of around 5×10^{17} cm^{-3} in the core of the filament [19]. Moreover, the pump peak power was several times higher than the self-focusing critical power for both the circularly and the linearly polarized pulses [20], resulting in a strong self-focusing. Consequently, the plasma density generated by the pump pulse (characterized by the N_2^+ fluorescence detected by a photomultiplier tube [19]) was nearly independent of the initial polarization state [see Fig. 4(a)] due to the dynamic equilibrium between the self-focusing and the self-generated plasma. However, the ionization yield of a circularly polarized NIR pulse is lower than for a linearly polarized laser pulse, and thus, the clamped laser intensity

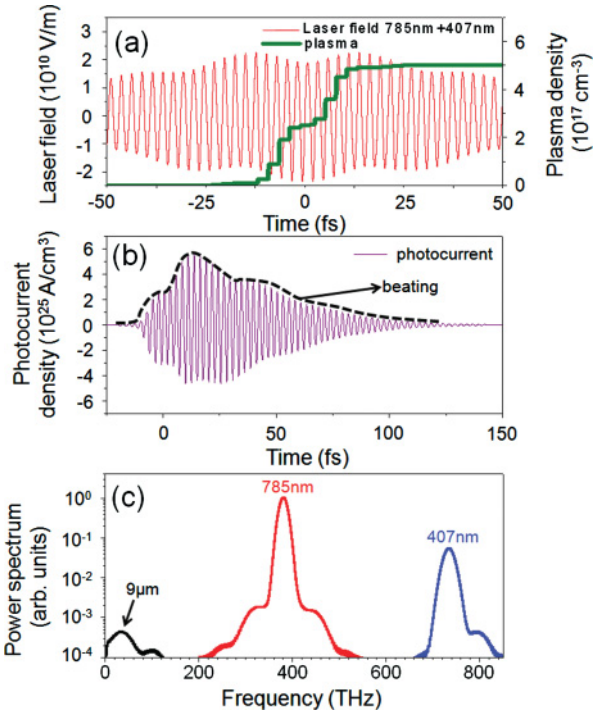

FIG. 3. (Color online) (a) Laser field amplitude (thin red line) and plasma density (thick green line) generated in air for a combined NIR and SH pulse with pulse widths of 50 and 70 fs, respectively. Both pump pulses were linearly polarized with peak intensity of $I_{\mathrm{NIR}} = 1.1 \times 10^{14}$ W/cm^2, and $I_{\mathrm{SH}} = 4 \times 10^{12}$ W/cm^2. (b) Time-varying photocurrent density on the filament axis. The dashed line represents the beating of the photocurrent envelope. (c) Power spectrum induced by the photocurrent from a 3-cm-long plasma filament with an on-axis peak plasma density of 5×10^{17} cm^{-3}. The arrow points out the peak wavelength of the generated FIR pulse (9 μm).

in the filament became dependent of the polarization state. According to the plasma density measured and the ionization rate of both O_2 and N_2, the retrieved laser intensity in the core of the filament was about 1.8×10^{14} and 1.1×10^{14} W/cm^2 for a circularly and a linearly polarized NIR laser pulse, respectively.

In simulations based on the 4WM model, only the $\chi^{(3)}_{xxxx}$ term contributes to the FIR-pulse generation when both SH and NIR pump pulses have linear and parallel polarizations. For a circularly polarized NIR pulse, the $\chi^{(3)}_{yxyx}$, $\chi^{(3)}_{xxyy}$, $\chi^{(3)}_{yxxy}$, and $\chi^{(3)}_{xxxx}$ terms would contribute to the FIR-pulse generation with the relation $\chi^{(3)}_{xxxx} = \chi^{(3)}_{yxyx} + \chi^{(3)}_{xxyy} + \chi^{(3)}_{yxxy}$. Consequently, the efficiency for the FIR-pulse generation with a circularly polarized NIR pulse is higher than for the linearly polarized case because the laser intensity is 1.6 times higher in the core of the filament and four $\chi^{(3)}$ terms [first bracket in Eq. (1)] can contribute to the parametric generation. Such behavior is demonstrated in Fig. 4(c) (black solid line), representing the calculated FIR-pulse energy generated through the 4WM mechanism by using the same f number as the experiments, an initial NIR pulse energy of 5 mJ (ten times the critical power for self-focusing [21]), and a SH pulse energy of 250 μJ. It should be noted that simulations with a NIR pulse having higher energy was not representative due to

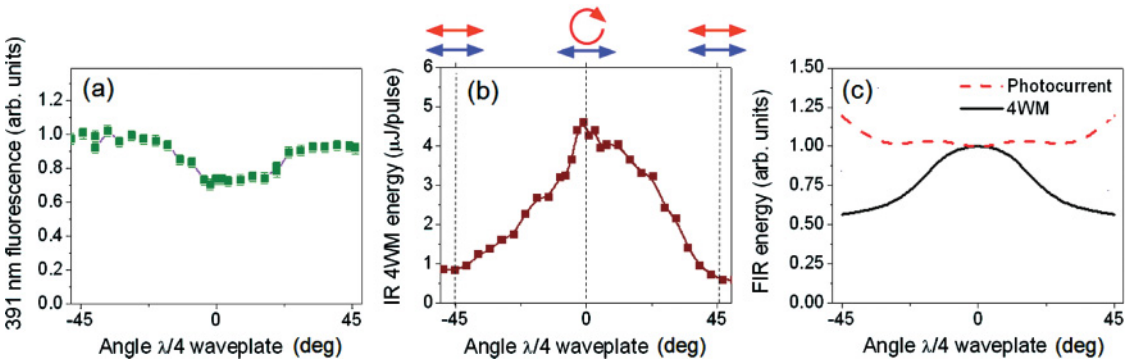

FIG. 4. (Color online) (a) N_2^+ fluorescence signal from the plasma column, and (b) FIR energy as a function of the quarter-wave plate angle for a 20-mJ NIR pulse. The energy of the linearly polarized SH pulse was 1 mJ. The zero angle corresponds to the circularly polarized NIR pulse and the $\pm 45^\circ$ angles are related to the linearly polarized NIR pulse. The red (upper) and blue (bottom) arrows in panel (b) depict the polarization state of the NIR and SH pulses, respectively. The FIR energy was measured with a calibrated germanium window and a long-pass wavelength filter (cutoff wavelength was 4 μm) in front of the mercury-cadmium-telluride detector. (c) Simulations of the FIR energy as a function of the NIR polarization state by using the 4WM (black line) and the photocurrent (red dashed line) models. Both simulations were normalized for the circularly polarized NIR pulse.

an overestimation of the plasma generation. Nevertheless, the 4WM simulations qualitatively match the experimental FIR-pulse energy measurements shown in Fig. 4(b).

In the photocurrent model, the physical process is less intuitive and careful approximations need to be done in the simulations. First, the photocurrent generation cannot be introduced into the slowly varying envelope approximation of the nonlinear Schrödinger equation because field ionization is required. Moreover, the temporal and spectral transformations of the pump pulses were limited since the tight focusing created a short filament of 3 cm long. For this reason, we approximated a constant laser intensity, pulse duration, and spatial profile in the filament zone for the photocurrent simulations. However, we extracted from the 4WM simulations the effective index of refraction along the filament (due to self-phase and cross-phase modulations) since the photocurrent is sensitive to the relative phase between the pump pulses [15]. Using these approximations and by considering the field ionization of both O_2 and N_2 in air, the simulations predict a quasiconstant energy for the FIR pulse as a function of the polarization state of the NIR pulse [see red dashed line in Fig. 4(c)]. Such constancy can be explained by the fact that the FIR-pulse generation through the photocurrent model depends mainly on the plasma density, which is weakly dependent of the polarization state [Fig. 4(a)] and the intensity of the SH pulse that was held constant. Moreover, the inherent drift of the relative phase between the SH and the NIR electric fields along the temporal profile averaged the photocurrent efficiency independently of the initial phase of the pump pulses and the fluctuation of the effective index of refraction along the filament. The experimental results in Fig. 4(b) differ from the ones obtained with the photocurrent simulations, which tends to confirm that the FIR-pulse generation in the two-color filamentation process is dominated by the 4WM mechanism.

In conclusion, during the filamentation of two-color nonharmonic laser pulses, the FIR-pulse generation can be the result of two potential mechanisms: the 4WM from the neutral molecules or the photocurrent beating in the plasma column. We observed experimentally that the FIR-pulse conversion efficiency with two-color nonharmonic pump pulses in air was higher with a circularly polarized NIR pump pulse and reached a notable energy conversion of $>2 \times 10^{-4}$. Such behavior corresponds well with the 4WM mechanism and its efficiency could be enhanced either with a gas medium like argon, which has a larger $\chi^{(3)}$ response and a similar ionization potential than air [12], or by using an optimal f number maximizing both the laser intensity and the volume of the filament [19]. Nevertheless, because of the results that we obtained, we cannot reject completely the possible impact of the photocurrent, but its contribution was weak, and the FIR-pulse generation was dominated by the 4WM process. Nowadays, the generation of both FIR and THz pulses finds wide applications in nonlinear optics, spectroscopy, and remote sensing. We expect that this finding could incite models of long-range filamentation where both the 4WM and the photocurrent models are involved and might seed each other.

ACKNOWLEDGMENTS

This work was supported in part by a Defence Research & Development Canada (DRDC) Technology Investment Fund and a DRDC Applied Research Program. The authors acknowledge technical support from Michèle Cardinal and Marcellin Jean.

[1] M. Rodriguez *et al.*, Opt. Lett. **27**, 772 (2002).
[2] M. Châteauneuf *et al.*, Appl. Phys. Lett. **92**, 091104 (2008).
[3] C. P. Hauri *et al.*, Appl. Phys. B **79**, 673 (2004).
[4] J. Kasparian *et al.*, Opt. Lett. **25**, 1397 (2000).
[5] F. Théberge *et al.*, Opt. Lett. **33**, 2515 (2008).
[6] J. Kasparian *et al.*, Science **301**, 61 (2003).
[7] S. L. Chin *et al.*, Can. J. Phys. **83**, 863 (2005).
[8] A. Couairon and A. Mysyrowicz, Phys. Rep. **441**, 47 (2007).

[9] J. Kasparian and J. P. Wolf, Opt. Express **16**, 466 (2008).
[10] Y. Zhang *et al.*, Opt. Express **16**, 15483 (2008).
[11] T. Fuji, T. Horio, and T. Suzuki, Opt. Lett. **32**, 2481 (2007).
[12] F. Théberge *et al.*, Phys. Rev. Lett. **97**, 023904 (2006).
[13] T. Fuji and T. Suzuki, Opt. Lett. **32**, 3330 (2007).
[14] D. J. Cook and R. M. Hochstrasser, Opt. Lett. **25**, 1210 (2000).
[15] K. Y. Kim *et al.*, Nat. Photonics **2**, 605 (2008).
[16] N. Karpowicz *et al.*, Appl. Phys. Lett. **92**, 011131 (2008).
[17] N. Aközbek *et al.*, Phys. Rev. Lett. **89**, 143901 (2002).
[18] J. Muth-Böhm, A. Becker, and F. H. M. Faisal, Phys. Rev. Lett. **85**, 2280 (2000).
[19] F. Théberge *et al.*, Phys. Rev. E **74**, 036406 (2006).
[20] S. Petit, A. Talebpour, A. Proulx, and S. L. Chin, Opt. Commun. **175**, 323 (2000).
[21] W. Liu and S. L. Chin, Opt. Express **13**, 5750 (2005).